A Control Methodology and Characterization of Dynamics for a Photovoltaic (PV) System Interfaced With a Distribution Network

Amirnaser Yazdani, *Member, IEEE*, and Prajna Paramita Dash, *Student Member, IEEE*

Abstract—This paper proposes a control strategy for a single-stage, three-phase, photovoltaic (PV) system that is connected to a distribution network. The control is based on an inner current-control loop and an outer dc-link voltage regulator. The current-control mechanism decouples the PV system dynamics from those of the network and the loads. The dc-link voltage-control scheme enables control and maximization of the real power output. Proper feedforward actions are proposed for the current-control loop to make its dynamics independent of those of the rest of the system. Further, a feedforward compensation mechanism is proposed for the dc-link voltage-control loop, to make the PV system dynamics immune to the PV array nonlinear characteristic. This, in turn, permits the design and optimization of the PV system controllers for a wide range of operating conditions. A modal/sensitivity analysis is also conducted on a linearized model of the overall system, to characterize dynamic properties of the system, to evaluate robustness of the controllers, and to identify the nature of interactions between the PV system and the network/loads. The results of the modal analysis confirm that under the proposed control strategy, dynamics of the PV system are decoupled from those of the distribution network and, therefore, the PV system does not destabilize the distribution network. It is also shown that the PV system dynamics are not influenced by those of the network (i.e., the PV system maintains its stability and dynamic properties despite major variations in the line length, line X/R ratio, load type, and load distance from the PV system).

Index Terms—Control, eigenvalue analysis, feedforward, modal analysis, participation factor, photovoltaic (PV), power electronics, voltage-source converter (VSC).

NOMENCLATURE

v_t	VSC ac-side terminal voltage.
v_s	VSC-filtered voltage; PCC voltage.
v_l	Load voltage.
v_g	Substation (grid) bus voltage.
v_{dc}	DC-link (PV array) voltage.
i	VSC ac-side current.
i_{g1}	Distribution line current between the PCC and load.
i_{g2}	Distribution line current between the load and substation.
i_l	Load current.
i_{pv}	PV array current.
P_{pv}	PV array power.
P_s	Real power output of the PV system at PCC.
Q_s	Reactive power output of the PV system at PCC.
N	Interface transformer turns ratio.
L	Inductance of the VSC interface reactor.
R	Resistance of the VSC interface reactor.
L_1	Line inductance between the PCC and load.
L_2	Line inductance between the load and substation.
R_1	Line resistance between the PCC and load.
R_2	Line resistance between the load and substation.
l_e	Line length.
d_f	Load distance from the PV system, normalized to line length.
C	DC-link capacitance.
C_f	Shunt capacitance at PCC; VSC filter capacitance.
C_l	Load power-factor correction capacitance.
ω	dq-frame angular speed.
ω_0	Grid nominal frequency (e.g., 377 rad/s).
ρ	dq-frame reference angle.
$Re\{\}$	Real part of.
$Im\{\}$	Imaginary part of.
$\sim$	Superscript denoting small-signal perturbation of a variable.
"0"	Subscript denoting the steady-state value of a variable.

$\wedge$	Superscript denoting the peak value of a three-phase variable.
$*$	Superscript denoting the complex-conjugate of a space phasor.
"T"	Superscript denoting the matrix transposition.
S	Solar irradiation level, normalized to 1.0 kW/m^2.
s	Complex frequency $\sigma + j\omega$.

I. Introduction

IN recent years, the concept of distributed generation (DG), which permits installation of relatively small-scale power generators at the medium-/low-voltage distribution levels of the power system, has gained widespread attention due to its technical, economical, and environmental benefits [1]. Among DG systems, photovoltaic (PV) solar systems have attracted considerable investment in several countries [2], such that significant penetration of the PV energy into distribution networks has already taken place in Europe, through single- and three-phase systems, and more penetration is anticipated worldwide. So far, PV systems of single- or double-digit megawatt (MW) capacities have been connected to the power system, mainly, at the subtransmission voltage levels. At the distribution voltage levels, most PV systems mainly consist of rooftop installations with capacities of a few kilowatts which are unlikely to make an impression on the distribution networks and the loads. These PV systems are not even permitted to cause a reverse power flow. This is, however, not the case for large-scale PV systems which have considerably higher capacities and more sophisticated controls. Thus, in view of the increasing market for multi-megawatt photvoltaic systems and in response to utility companies concerns about the impact of large-scale PV systems on the feeders/customers, investigations on the control, dynamic properties, transient performance, and interactions with the network/loads of large-scale distributed PV systems seem to be timely and of importance.

Many previous works have investigated different aspects of PV systems, including the energy production and economics [3]–[5]. The most widely addressed technical issue regarding PV systems is the so-called maximum power-point tracking (MPPT). Reference [6] reviews 19 different MPPT methods introduced since 1968. The scope of the reported works encompasses both large-scale and distributed PV systems. Another widely addressed topic is that of power converter configurations and aggregation schemes for PV systems. References [7]–[10] provide comprehensive surveys on different single-phase and three-phase converter circuits for PV applications. Recently, with the consideration of PV systems as DG units, research works also report the integration of islanding detection schemes into single-phase PV systems [11]–[14]. In addition, a fair amount of the technical literature has dealt with the integration of PV systems into distribution networks. The majority of this body of the literature has focused on single-phase PV systems, with an emphasis on their harmonic interactions with the distribution networks [15]–[17] and on their impact on the power quality (PQ) [18]–[20]. Research has also dealt with

transformer overload and feeder overvoltage issues. However, only a few previous works have investigated the control and stability aspects of PV systems.

Dynamic stability of single-phase, distributed PV systems is investigated in [21] and [22]. Reference [21] has conducted an eigenvalue analysis for a two-stage configuration, with the model of the dc cable between the two stages considered. However, the distribution line and loads are not modeled. Reference [22] has studied the impact of grid impedance variations on the closed-loop stability of a single-phase PV system. Moreover, a control design methodology to ensure the provision of adequate damping has been presented.

A number of works have studied dynamic models, stability, and/or the control of three-phase, single-stage PV systems [25]–[28]. Reference [25] has elegantly developed a reduced-order model for a PV system; the model and the proposed controllers are based on the voltage-mode control strategy, and they can be conveniently incorporated into time-domain power system simulation studies. This paper, however, does not provide a stability analysis or controller design methodology.

A number of works [26]–[28] have adopted the current-mode control strategy. Reference [26] identifies the control loops and the transfer functions of the PV system, but does not report any analysis of the stability or interactions with the line/loads. Reference [27] has adopted a similar analysis approach as in [26], with an emphasis on the impact of grid impedance on the closed-loop stability and not on the interaction between the PV system and the distribution network. In [28], the behavior of a three-phase, single-stage PV system has been studied, with an emphasis on the MPPT strategy rather than on the control or stability of the PV system.

This paper proposes an effective control strategy for a single-stage, three-phase PV system which is connected to a distribution network. The proposed control strategy is based on a modified version of the conventional current-mode control and is used to 1) regulate the PV system power factor and 2) to control the converter dc-link voltage and, therefore, the PV system real-power output, through a dc-link voltage-control scheme. In addition to protecting the PV system against external faults, the modified current-control strategy virtually decouples the PV system from the distribution network and the loads, as analytically shown in this paper. The dc-link voltage-control scheme, on the other hand, ensures stable operation of the PV system, guarantees safe operation of the voltage-source converter (VSC) of the PV system, and permits incorporation of an MPPT scheme. This paper also proposes a feedforward compensation strategy for the dc-link voltage-control loop, to eliminate the impact of the nonlinear characteristics of the PV panels on the closed-loop stability. The proposed feedforward compensation permits the design of the dc-link voltage controller irrespective of the PV system operating point, and also renders the closed-loop eigenvalues of the PV system insensitive to solar irradiation and dc-link voltage levels. The effectiveness of the proposed control strategy, and its robustness against changes in the operating conditions, distribution network parameters, and load types/parameters are demonstrated through nonlinear, time-domain simulations as well as a comprehensive modal analysis.
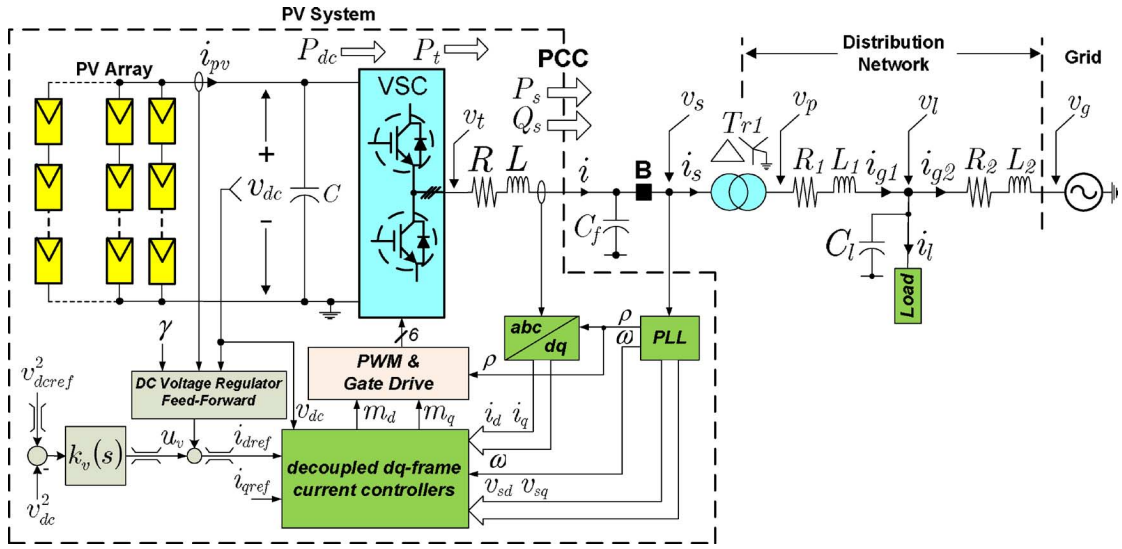
Fig. 1. Single-line schematic diagram of a single-stage photovoltaic (PV) system interfaced with a distribution network.

The rest of this paper is organized as follows. Section II introduces the structure of the single-stage, three-phase PV system. Sections III and IV present a mathematical model and the controllers of the PV system. In Section V, a small-signal model for the overall system consisting of the PV system, the distribution network, and the load(s) is developed and verified. Section V also presents the result of a modal analysis carried out on the linearized model of the overall system. Section VI concludes this paper.

II. STRUCTURE OF THE PV SYSTEM

Fig. 1 shows a single-line schematic diagram of a three-phase, single-stage PV system interfaced with a distribution network at the point of common coupling (PCC). The main building blocks of the PV system are an array of PV panels, a VSC, and a three-phase interface reactor. The array of PV panels, hereafter referred to as the PV array, is composed of the parallel connection of n_p strings of panels to ensure adequately large power. In turn, to ensure an adequately large dc voltage, each string consists of a number of PV panels connected in series; this, in total, corresponds to n_s series-connected PV cells. The PV array is connected in parallel to the dc-link capacitor C and the dc-side terminals of the VSC. The VSC is controlled based on the sinusoidal pulse-width modulation (SPWM) strategy. The interface reactor connects the ac-side terminals of the VSC to the corresponding phases of the PCC. The resistance and inductance of the interface reactor are represented by L and R, respectively. R also includes the resistance of the VSC valves. P_s and Q_s represent the real- and reactive-power output that the PV system delivers to the distribution network. In emergency conditions when the PV system must be shut down, the breaker B isolates the PV system from the distribution network.

Fig. 1 also includes a schematic diagram of the distribution network and an aggregate of loads. In this paper, the distribution network is referred to as the composition of a distribution line, the transformer T_{r1}, and the shunt capacitors C_f and C_l. T_{r1} steps down the network voltage to a level suitable for the PV

system. The high-voltage side of T_{r1} has a *wye* winding configuration and is solidly grounded. C_f provides a low-impedance path for the current harmonics generated by the PV system, and prevents them from penetrating into the distribution network.

As Fig. 1 shows, the distribution network is supplied by a utility substation which is represented by the voltage source v_g. In addition, a (three-phase) load is connected to the line at a location between the PCC and the substation. The inductance and resistance of the distribution line segment between the PCC and the load are represented by L_1 and R_1, respectively. L_1 and R_1 also include the leakage inductance and the winding resistance of T_{r1}, respectively. Similarly, L_2 and R_2, respectively, represent the inductance and resistance of the line segment between the load and the substation. It should be pointed out that, for the purpose of analysis in this paper, C_f and C_l are considered parts of the distribution network. However, practically, the former is an integral component of the VSC filter, whereas the latter represents the load power-factor correction capacitor.

III. LARGE-SIGNAL MODEL

A. PV System Model

The PV array is described by its current–voltage characteristic function, as [29]

$$i_{\text{pv}} = n_p I_{ph} - n_p I_{rs} \left[\exp \left(\frac{q}{k\vartheta A} \frac{v_{dc}}{n_s} \right) - 1 \right] \quad (1)$$

where I_{rs} is the reverse saturation current of a $p - n$ junction, $q(= 1.602 \times 10^{-19}$ C) is the unit electric charge, $k(= 1.38 \times 10^{-23}$ J/K) is Boltzman's constant, ϑ is the $p - n$ junction temperature (in Kelvin), A is the ideality factor, and I_{ph} is the short-circuit current of one string of the PV panels. I_{ph}, a function of the temperature, is a linear function of the solar irradiation level S, as

$$I_{ph} = [I_{scr} + k_\vartheta (\vartheta - \vartheta_r)] \frac{S}{100} \quad (2)$$

where ϑ_r is the cell reference temperature, I_{scr} is the short-circuit current of one PV cell at the reference temperature and
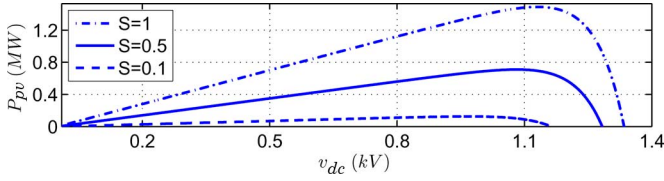
Fig. 2. Power-voltage characteristic curve of a PV array.

irradiation level, and k_ϑ is a temperature coefficient. Based on (1), the power delivered by the PV array (i.e., $P_{pv} = i_{pv}v_{dc}$) is expressed as

$$P_{pv} = f(v_{dc}, S, \vartheta)$$
$$= n_p I_{ph}v_{dc} - n_p I_{rs}v_{dc}\left[\exp\left(\frac{q}{k\vartheta A}\frac{v_{dc}}{n_s}\right) - 1\right]. \quad (3)$$

Fig. 2 illustrates the variations of P_{pv} as a function of v_{dc}, for different levels of the solar irradiation. Fig. 2 shows that for a given irradiation level, P_{pv} is zero at $v_{dc} = 0$ but increases as v_{dc} is increased. However, this trend continues only up to a certain voltage at which P_{pv} reaches a peak value; beyond this voltage, P_{pv} decreases with the increase of v_{dc}. The aforementioned behavior suggests that P_{pv} can be controlled/maximized by the control of v_{dc}. This is referred to as the "maximum-power-point tracking" (MPPT) in the technical literature [6].

Dynamics of the dc-link voltage are described, based on the principle of power balance, as

$$\frac{C}{2}\frac{dv_{dc}^2}{dt} = \underbrace{f(v_{dc}, S, \vartheta)}_{P_{pv}} - P_{dc} \quad (4)$$

where P_{dc} denotes the power delivered to the VSC dc side (see Fig. 1). Ignoring the VSC power loss, P_{dc} can be assumed to be equal to P_t, that is, the real component of the VSC ac-side terminal power. P_t, in turn, is the summation of P_s and the real power absorbed by the interface reactor [30]. Thus

$$P_{dc} \approx P_t = \underbrace{\frac{3}{2}Re\{\overrightarrow{v_s}\,\overrightarrow{i}^*\}}_{P_s} + \underbrace{\frac{3}{2}Re\{R\,\overrightarrow{i}\,\overrightarrow{i}^*\}}_{P_R}$$
$$+ \underbrace{\frac{3}{2}Re\left\{L\frac{d\overrightarrow{i}}{dt}\overrightarrow{i}^*\right\}}_{P_L} \quad (5)$$

where $\overrightarrow{x}$ denotes the space-phasor representation of a three-phase quantity $x_{abc}(t)$ and is defined as [31]

$$\overrightarrow{x} = \frac{2}{3}\left(x_a e^{j0} + x_b e^{j\frac{2\pi}{3}} + x_c e^{j\frac{4\pi}{3}}\right). \quad (6)$$

Substituting for P_{dc} from (5) in (4), one deduces

$$\frac{C}{2}\frac{dv_{dc}^2}{dt} = \underbrace{f(v_{dc}, S, \vartheta)}_{P_{pv}} - \underbrace{\frac{3}{2}Re\{\overrightarrow{v_s}\,\overrightarrow{i}^*\}}_{P_s} - \frac{3}{2}Re\{R\,\overrightarrow{i}\,\overrightarrow{i}^*\}$$
$$- \frac{3}{2}Re\left\{L\frac{d\overrightarrow{i}}{dt}\overrightarrow{i}^*\right\}. \quad (7)$$

Equation (7) suggests that v_{dc} and, thus, P_{pv} can be controlled by the VSC ac-side current $\overrightarrow{i}$. It should also be noted that (7) represents a nonlinear dynamic system, due to the nonlinear dependence of P_{pv} on v_{dc} (see (3) and Fig. 2) as well as the presence of the terms $\overrightarrow{v_s}\,\overrightarrow{i}^*$, $\overrightarrow{i}\,\overrightarrow{i}^*$, and $(d\overrightarrow{i}/dt)\overrightarrow{i}^*$.

The dynamics of the VSC ac-side current are described by the following space-phasor equation:

$$L\frac{d\overrightarrow{i}}{dt} = -R\overrightarrow{i} + \overrightarrow{v_t} - \overrightarrow{v_s} \quad (8)$$

$\overrightarrow{v_t}$, that is, the VSC ac-side terminal voltage can be controlled as

$$\overrightarrow{v_t} = \frac{v_{dc}}{2}\overrightarrow{m} \quad (9)$$

where $\overrightarrow{m}$ represents the space-phasor corresponding to the PWM modulating signals which are normalized to the peak value of the triangular carrier signal. Substituting for $\overrightarrow{v_t}$ from (9) in (8), one deduces

$$L\frac{d\overrightarrow{i}}{dt} = -R\overrightarrow{i} + \frac{v_{dc}}{2}\overrightarrow{m} - \overrightarrow{v_s}. \quad (10)$$

Equations (7) and (10) constitute a state-space model for the PV system in which v_{dc}^2 and $\overrightarrow{i}$ are the state variables, $\overrightarrow{m}$ is the control input, and $\overrightarrow{v_s}$ and S are the exogenous inputs. It should be noted that $\overrightarrow{v_s}$ itself is a state variable of the distribution network system, as discussed in the next subsection.

B. Distribution Network Model

If $\overrightarrow{v_s}$, $\overrightarrow{v_l}$, $\overrightarrow{i_{g1}}$, and $\overrightarrow{i_{g2}}$ are chosen as the state variables, the following state-space model can be derived for the distribution network:

$$C_f\frac{d\overrightarrow{v_s}}{dt} = \overrightarrow{i} - \underbrace{N\overrightarrow{i_{g1}}}_{\overrightarrow{i_s}} \quad (11)$$

$$C_l\frac{d\overrightarrow{v_l}}{dt} = \overrightarrow{i_{g1}} - \overrightarrow{i_{g2}} - \overrightarrow{i_l} \quad (12)$$

$$L_1\frac{d\overrightarrow{i_{g1}}}{dt} = -R_1\overrightarrow{i_{g1}} + \underbrace{N\overrightarrow{v_s}}_{\overrightarrow{v_p}} - \overrightarrow{v_l} \quad (13)$$

$$L_2\frac{d\overrightarrow{i_{g2}}}{dt} = -R_2\overrightarrow{i_{g2}} + \overrightarrow{v_l} - \underbrace{\widehat{v}_g e^{j\omega_0 t}}_{\overrightarrow{v_g}} \quad (14)$$

where the PV system ac-side current $\overrightarrow{i}$ and the load current $\overrightarrow{i_l}$ act as exogenous inputs to the distribution network subsystem. In (14), it is assumed that $v_{gabc}(t)$ is a balanced three-phase voltage whose amplitude and phase angle are $\widehat{v}_g$ and $\omega_0 t$, respectively.

C. Load Model

Three types of three-phase, balanced loads—an asynchronous machine, a series $R-L$ circuit, and a thyristor-bridge

rectifier are considered in this paper. A space-phasor model of an asynchronous machine can be found in [31] or [32]. The model can be expressed in the standard state-space form, through minor algebra, which is not presented here for space limitations. The procedures to derive the state-space models of the $R - L$ load and the rectifier load are presented in detail in Appendix A.

IV. PV System Control

For the PV system of Fig. 1, the main control objective is to regulate the dc-link voltage to control/maximize the power extracted from the PV array. Fig. 1 indicates that: 1) the VSC PWM and control are synchronized to the network voltage through a phase-locked loop (PLL) [33]. Thus, the three-phase ac signals are transformed into proper dq-frame counterparts, and the controllers process dc equivalents rather than original sinusoidally-varying signals and 2) the error between (the square of) the dc-link voltage and its corresponding reference value is processed by the compensator $k_v(s)$ whose output is augmented by a feedforward signal to issue the current command i_{dref}. The feedforward compensation counteracts the destabilizing and nonlinear characteristic of the PV array and enhances the PV system stability. The dc-link voltage reference is usually obtained from an MPPT scheme and is permitted to vary from a lower limit to an upper limit. The limits on the dc-link voltage ensure proper and safe operation of the VSC; and 3) the command i_{dref} is delivered to a dq-frame current-control scheme that forces i_d to track i_{dref}. The control of i_d enables the control of P_s and P_{pv}. A saturation block limits i_{dref} to protect the VSC against overload and external faults. The current-control scheme also forces i_q to track i_{qref}. It is also discussed in Section IV-A that Q_s is proportional to i_q. Hence, if $i_{\text{qref}} = 0$, Q_s becomes zero in the steady state and the PV system exhibits a unity power factor to the distribution network. The unity power-factor operation also results in a minimized magnitude for the VSC line current, for a given real-power flow.

Details of the aforementioned three control schemes are discussed in the following subsections.

A. Phase-Locked Loop (PLL)

For analysis and control purposes, space-phasor variables in the models of the PV system, the distribution network, and the load are projected on a dq-frame. This is achieved by replacing each space phasor by its dq-frame equivalent, as

$$\overrightarrow{x} = (x_d + jx_q)e^{j\rho}. \tag{15}$$

If $\overrightarrow{x}$ represents a state variable, $d\overrightarrow{x}/\text{dt}$ is calculated as

$$\frac{d\overrightarrow{x}}{\text{dt}} = \left(\frac{dx_d}{\text{dt}} + j\frac{dx_q}{\text{dt}}\right)e^{j\rho} + j\omega(t)(x_d + jx_q)e^{j\rho} \tag{16}$$

where ω is the dq-frame angular speed, as

$$\omega = \frac{d\rho}{\text{dt}}. \tag{17}$$
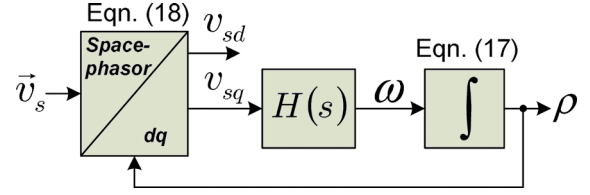

Fig. 3. Block diagram of a phase-locked loop (PLL).

The space phasor to the dq-frame transformation is defined as

$$x_d + jx_q = \overrightarrow{x}e^{-j\rho}. \tag{18}$$

In the system of Fig. 1, the three-phase signals vary with time at the grid frequency ω_0. Therefore, the dq-frame variables become time invariant (in a steady state) if the dq-frame angular velocity ω is made to be equal to ω_0. This objective is fulfilled by means of the PLLs of Fig. 3, [33], in which $\overrightarrow{v_s}$ is first resolved into the d- and the q-axis components, based on (18), and then v_{sq} is processed by the compensator $H(s)$ to determine ω. In a steady state, v_{sq} is forced to zero while ω becomes equal to ω_0. Therefore, $H(s)$ must include at least one integrator (i.e. one pole at $s = 0$).

Let $H(s)$ be a proportional-integral (PI) compensator cascaded with a first-order, low-pass transfer-function, as

$$\Omega(s) = H(s)V_{sq}(s) = \frac{\beta_1 s + \beta_2}{s(s + \beta_3)}V_{sq}(s) \tag{19}$$

where $\Omega(s)$ and $V_{sq}(s)$ are the Laplace transforms of $\omega(t)$ and $v_{sq}(t)$, respectively. If the two state variables $\zeta_1(t) = \mathcal{L}^{-1}\{Z_1(s)\}$ and $\zeta_2(t) = \mathcal{L}^{-1}\{Z_2(s)\}$ are defined as

$$Z_2(s) = \frac{V_{sq}(s)}{s^2 + \beta_3 s} \tag{20}$$

$$Z_1(s) = sZ_2(s) \tag{21}$$

then, in view of (17), the following state-space model can be formulated for the PLL:

$$\frac{d}{\text{dt}}\mathbf{X}_{\text{pll}} = \mathbf{A}_{\text{pll}}\mathbf{X}_{\text{pll}} + \mathbf{B}_{\text{pll}}\begin{bmatrix} v_{sd} \\ v_{sq} \end{bmatrix} \tag{22}$$

$$\omega = \mathbf{E}_{\text{pll}}\mathbf{X}_{\text{pll}} \tag{23}$$

$$\rho = \mathbf{F}_{\text{pll}}\mathbf{X}_{\text{pll}} \tag{24}$$

where

$$\mathbf{A}_{\text{pll}} = \begin{bmatrix} -\beta_3 & 0 & 0 \\ 1 & 0 & 0 \\ \beta_1 & \beta_2 & 0 \end{bmatrix} \tag{25}$$

$$\mathbf{B}_{\text{pll}} = \begin{bmatrix} 0 & 1 \\ 0 & 0 \\ 0 & 0 \end{bmatrix} \tag{26}$$

$$\mathbf{E}_{\text{pll}} = \begin{bmatrix} \beta_1 & \beta_2 & 0 \end{bmatrix} \tag{27}$$

$$\mathbf{F}_{\text{pll}} = \begin{bmatrix} 0 & 0 & 1 \end{bmatrix} \tag{28}$$

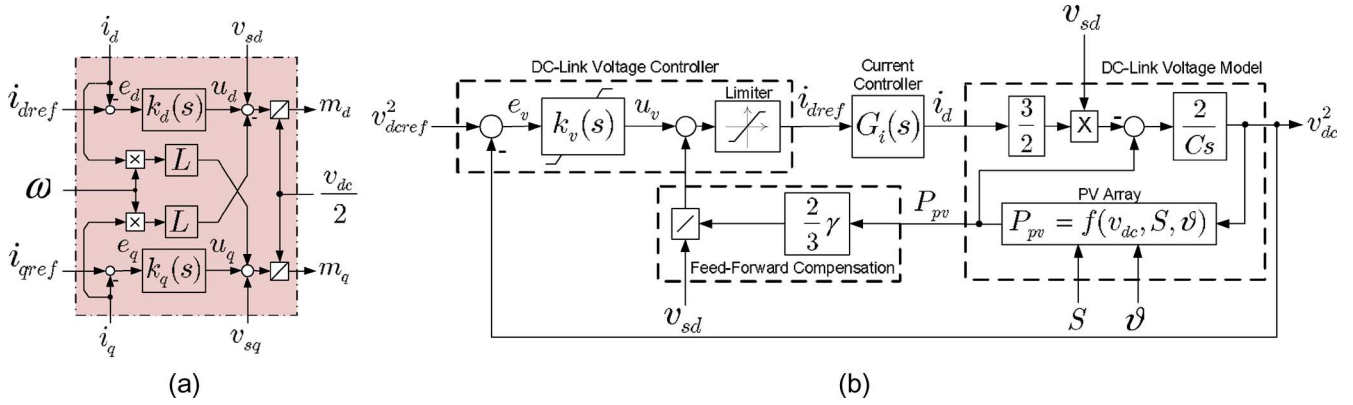$$\mathbf{X}_{\text{pll}} = \begin{bmatrix} \zeta_1 & \zeta_2 & \rho \end{bmatrix}^T. \tag{29}$$

Fig. 4. Block diagrams of (a) dq-frame current-control scheme. (b) DC-link voltage-control scheme.

Equations (22)–(24) introduce the PLL as a dynamic system of which the inputs are v_{sd} and v_{sq}; the state variables are ζ_1, ζ_2, and ρ; and the outputs are ω and ρ.

Regulation of v_{sq} at zero also has the effect that the expression for the PV system real-power output (i.e., $P_s = (3/2)Re\{\overrightarrow{v_s}\,\overrightarrow{i}^*\}$) is simplified to

$$P_s = \frac{3}{2}v_{sd}i_d. \tag{30}$$

Equation (30) indicates that P_s is proportional to and can be controlled by i_d. As indicated in (7), P_s is controlled to regulate the dc-link voltage and to control/maximize the power extracted from the PV array. Consequently, the control of P_s boils down to the control of i_d, as illustrated in Fig. 1. Similarly, the expression for Q_s is simplified to

$$Q_s = \frac{3}{2}Im\{\overrightarrow{v_s}\,\overrightarrow{i}^*\} = -\frac{3}{2}v_{sd}i_q. \tag{31}$$

Thus, Q_s can be regulated by i_q to adjust the power factor that the PV system exhibits to the distribution network.

B. VSC Current Control

The need for controlling i_d and i_q was explained in Section IV-A. In this section, a current-control scheme is devised to ensure that i_d and i_q rapidly track their respective reference commands i_{dref} and i_{qref}. The current-control strategy also enhances protection of the VSC against overload and external faults, provided that i_{dref} and i_{qref} are limited.

The current-control scheme is designed based on (32) and (33) which are the dq-frame equivalents to (10). Thus

$$L\frac{di_d}{dt} = -Ri_d + L\omega i_q + \frac{v_{dc}}{2}m_d - v_{sd} \tag{32}$$

$$L\frac{di_q}{dt} = -Ri_q - L\omega i_d + \frac{v_{dc}}{2}m_q - v_{sq}. \tag{33}$$

In (32) and (33), i_d and i_q are the state variables and the outputs, m_d and m_q are the control inputs, and v_{sd} and v_{sq} are the disturbance inputs. Due to the factor $L\omega$, the dynamics of i_d and i_q are coupled and nonlinear. To decouple and linearize the dynamics,

m_d and m_q are determined based on the following control laws:

$$m_d = \frac{2}{v_{dc}}(u_d - L\omega i_q + v_{sd}), \tag{34}$$

$$m_q = \frac{2}{v_{dc}}(u_q + L\omega i_d + v_{sq}) \tag{35}$$

where u_d and u_q are two new control inputs [34]. Substituting m_d and m_q in (32) and (33), respectively, from (34) and (35), one deduces

$$L\frac{di_d}{dt} = -Ri_d + u_d \tag{36}$$

$$L\frac{di_q}{dt} = -Ri_q + u_q. \tag{37}$$

Equations (36) and (37) represent two, decoupled, linear, first-order systems in which i_d and i_q can be controlled by u_d and u_q, respectively. Fig. 4(a) illustrates a block diagram of the dq-frame current-control scheme [i.e., a realization of (34) and (35)]. Fig. 4(a) shows that the control signal u_d is the output of a compensator $k_d(s)$, processing the error signal $e_d = i_{dref} - i_d$. Similarly, u_q is the output of another compensator $k_q(s)$ that processes $e_q = i_{qref} - i_q$. It should be noted that to produce m_d and m_q, the factor $2/v_{dc}$ is employed as a feedforward signal to decouple the dynamics of i_d and i_q from those of v_{dc}. The PWM modulating signals are generated by transformation of m_d and m_q into m_a, m_b, and m_c [not shown in Fig. 4(a)], and the gating pulses for the VSC valves are sent out.

Since the control plants of (36) and (37) are identical, $k_d(s)$ and $k_q(s)$ can also be identical. Let

$$k_d(s) = k_q(s) = \frac{k_p s + k_i}{s} \tag{38}$$

where k_p and k_i are the proportional and integral gains, respectively. If k_p and k_i are selected as

$$k_p = \frac{L}{\tau_i} \tag{39}$$

$$k_i = \frac{R}{\tau_i} \tag{40}$$

then the closed-loop transfer functions of the d- and q-axis current controllers assume the first-order form

$$\frac{I_d(s)}{I_{\text{dref}}(s)} = \frac{I_q(s)}{I_{\text{qref}}(s)} = G_i(s) = \frac{1}{\tau_i s + 1} \quad (41)$$

where the time-constant τ_i should be made small for a fast current-control response, but adequately large so that $1/\tau_i$ (i.e., the bandwidth of the closed current-control loop) is considerably (e.g. ten times) smaller than the VSC switching frequency (in radians per second). In this paper, τ_i is equal to 0.5 ms. It is noted that the foregoing control method renders the dynamics of i_d and i_q decoupled from those of ω, v_{dc}, v_{sd}, and v_{sq}.

C. DC-Link Voltage Control

The DC-link voltage is controlled by i_d, based on the model of (7) whose dq-frame equivalent is

$$\frac{C}{2}\frac{dv_{\text{dc}}^2}{dt} = f(v_{\text{dc}}, S, \vartheta) - \frac{3}{2}(v_{sd}i_d + v_{sq}i_q) \\ - \frac{3}{4}L\left(\frac{di_d^2}{dt} + \frac{di_q^2}{dt}\right) - \frac{3}{2}R\left(i_d^2 + i_q^2\right). \quad (42)$$

In (42), the first and second terms represent the (real) power delivered by the PV array and the PV system, respectively. The third and fourth terms, respectively, represent the power absorbed by the inductance and the resistance of the VSC interface reactor. Ignoring the third and fourth terms of (42), and considering that v_{sq} is regulated at zero by the PLL, a reduced-order model is obtained for the dc-link voltage dynamics as

$$\frac{C}{2}\frac{dv_{\text{dc}}^2}{dt} \approx f(v_{\text{dc}}, S, \vartheta) - \frac{3}{2}v_{sd}i_d \\ \approx f(v_{\text{dc}}, S, \vartheta) - \frac{3}{2}v_{sd}i_{\text{dref}}. \quad (43)$$

Equation (43) represents a control plant whose input is i_{dref}, assuming that the time-constant τ_i in (41) is so small that $i_d \approx i_{\text{dref}}$ holds. In (43), v_{dc}^2 is the state variable as well as the output and v_{sd} is an exogenous input (disturbance). The control plant of (43) is nonlinear since 1) $P_{\text{pv}} = f(v_{\text{dc}}, S, \vartheta)$ is a nonlinear function of v_{dc}, and 2) v_{dc} itself is a nonlinear function of the state-variable v_{dc}^2. To mitigate the impact of nonlinearities on the control, the following control law is adopted for i_{dref}:

$$i_{\text{dref}} = u_v + \gamma \frac{P_{\text{pv}}}{\frac{3}{2}v_{sd}} \quad (44)$$

where u_v is a new control input, and γ is a gain which can be unity or zero. $P_{\text{pv}} = f(v_{\text{dc}}, S, \vartheta)$ is calculated from the product of v_{dc} and i_{pv}. The substitution of i_{dref} from (44) in (43) yields

$$\frac{C}{2}\frac{dv_{\text{dc}}^2}{dt} \approx (1 - \gamma)f(v_{\text{dc}}, S, \vartheta) - \frac{3}{2}v_{sd}u_v. \quad (45)$$

Equation (45) indicates that if $\gamma = 1$, the impact of the PV array characteristic on the dc-link voltage control is eliminated, and the effective control plant becomes an integrator. Although the

product $v_{sd}u_v$ also introduces a nonlinearity, its impact is insignificant since practically v_{sd} is a relatively constant variable. u_v is the output of a compensator as

$$U_v(s) = k_v(s)E_v(s) = \frac{\alpha_1 s + \alpha_2}{s(s + \alpha_3)}E_v(s) \quad (46)$$

where the error signal is $e_v = v_{\text{dcref}}^2 - v_{\text{dc}}^2$. Equation (46) represents a PI compensator cascaded with a first-order low-pass filter. α_1 and α_2 are, respectively, the proportional and integral gains of the PI compensator, whereas α_3 is the pole of the low-pass transfer function.

Fig. 4(b) illustrates a block diagram of the dc-link voltage-control scheme described before. It is noted that if $\gamma = 1$, the effective control plant from u_v to v_{dc}^2 is composed of an integrator cascaded with the first-order transfer-function $G_i(s)$. For such a plant, the method of "symmetrical optimum" provides a systematic tool for calculating the parameters of a PI compensator [32] and is utilized in this paper.

V. STABILITY ANALYSIS

To evaluate the stability of the PV system under the proposed control strategy and to investigate the potential for interactions between the PV system and the distribution network/load, an eigenvalue analysis is carried out on a linearized state-space model of the overall system. The linear model parameters are functions of the steady-state operating point of the system. For the purposes of modeling and analysis, the system of Fig. 1 is divided into four subsystems. The subsystems are: 1) the PLL subsystem, 2) the converter subsystem, 3) the distribution network subsystem, and 4) the load subsystem. The linearized models of the aforementioned subsystems are discussed next.

A. Linearized Model

1) Linearized Model of the PLL Subsystem: The PLL subsystem is described by (22)–(24) which are linear. Therefore, the linearized model of the PLL subsystem also preserves the forms of (22)–(24) as

$$\frac{d}{dt}\widetilde{\mathbf{X}}_{\text{pll}} = \mathbf{A}_{\text{pll}}\widetilde{\mathbf{X}}_{\text{pll}} + \mathbf{B}_{\text{pll}}\begin{bmatrix}\widetilde{v}_{sd} \\ \widetilde{v}_{sq}\end{bmatrix} \quad (47)$$

$$\widetilde{\omega} = \mathbf{E}_{\text{pll}}\widetilde{\mathbf{X}}_{\text{pll}} \quad (48)$$

$$\widetilde{\rho} = \mathbf{F}_{\text{pll}}\widetilde{\mathbf{X}}_{\text{pll}} \quad (49)$$

where

$$\widetilde{\mathbf{X}}_{\text{pll}} = [\widetilde{\zeta}_1 \quad \widetilde{\zeta}_2 \quad \widetilde{\rho}]^T. \quad (50)$$

Equations (47)–(49) describe the PLL as a subsystem for which $\widetilde{v}_{sd}$ and $\widetilde{v}_{sq}$ are the inputs obtained from the distribution network subsystem, $\widetilde{\omega}$ is the output delivered to the distribution network and load subsystems, and $\widetilde{\rho}$ is the output delivered to the distribution network subsystem.

2) Linearized Model of the Converter Subsystem: The converter subsystem is referred to as the composition of the PV array, the VSC in conjunction with the dc-link capacitor and the interface reactor, the current-control scheme, and the dc-link voltage regulator. A linearized model of the converter

subsystem is developed based on (3), (41), (42), (44), and (46). The process yields

$$\frac{d}{dt}\widetilde{\mathbf{X}}_c = \mathbf{A}_c\widetilde{\mathbf{X}}_c + \mathbf{B}_c\begin{bmatrix}\widetilde{v}_{sd}\\\widetilde{v}_{sq}\end{bmatrix} + \mathbf{C}_c\begin{bmatrix}\widetilde{v}_{dcref}\\\widetilde{i}_{qref}\end{bmatrix} \quad (51)$$

$$\begin{bmatrix}\widetilde{i}_d\\\widetilde{i}_q\end{bmatrix} = \mathbf{E}_c\widetilde{\mathbf{X}}_c \quad (52)$$

where

$$\widetilde{\mathbf{X}}_c = \begin{bmatrix}\widetilde{i}_d & \widetilde{v}_{dc} & \widetilde{x}_3 & \widetilde{x}_4 & \widetilde{i}_q\end{bmatrix}^T. \quad (53)$$

In (53), $\widetilde{x}_3$ and $\widetilde{x}_4$ are the state variables of the compensator $k_v(s)$.

Equations (51) and (52) constitute a linearized model for the converter subsystem. The equations indicate that $\widetilde{v}_{sd}$ and $\widetilde{v}_{sq}$ are the inputs obtained from the distribution network subsystem, while $\widetilde{i}_d$ and $\widetilde{i}_q$ are the outputs delivered to the distribution network subsystem.

3) Linearized Model of the Distribution Network Subsystem: Based on (11)–(14), a linearized model for the distribution network assumes the form

$$\frac{d}{dt}\widetilde{\mathbf{X}}_n = \mathbf{A}_n\widetilde{\mathbf{X}}_n + \mathbf{B}_n\begin{bmatrix}\widetilde{i}_d\\\widetilde{i}_q\end{bmatrix} + \mathbf{C}_n\widetilde{\omega} + \mathbf{H}_n\widetilde{\rho} + \mathbf{D}_n\begin{bmatrix}\widetilde{i}_{ld}\\\widetilde{i}_{lq}\end{bmatrix} \quad (54)$$

$$\begin{bmatrix}\widetilde{v}_{ld}\\\widetilde{v}_{lq}\end{bmatrix} = \mathbf{E}_n\widetilde{\mathbf{X}}_n \quad (55)$$

$$\begin{bmatrix}\widetilde{v}_{sd}\\\widetilde{v}_{sq}\end{bmatrix} = \mathbf{F}_n\widetilde{\mathbf{X}}_n \quad (56)$$

where

$$\widetilde{\mathbf{X}}_n = \begin{bmatrix}\widetilde{i}_{g1d} & \widetilde{i}_{g1q} & \widetilde{i}_{g2d} & \widetilde{i}_{g2q} & \widetilde{v}_{sd} & \widetilde{v}_{sq} & \widetilde{v}_{ld} & \widetilde{v}_{lq}\end{bmatrix}. \quad (57)$$

Equations (54)–(56) describe the distribution network as a subsystem for which $\widetilde{i}_d$ and $\widetilde{i}_q$ are the inputs obtained from the converter subsystem, $\widetilde{i}_{ld}$ and $\widetilde{i}_{lq}$ are the inputs obtained from the load subsystem, and $\widetilde{\omega}$ and $\widetilde{\rho}$ are the inputs obtained from the PLL subsystem. On the other hand, $\widetilde{v}_{ld}$ and $\widetilde{v}_{lq}$ are the outputs delivered to the load subsystem; and $\widetilde{v}_{sd}$ and $\widetilde{v}_{sq}$ are the outputs delivered to the PLL and converter subsystems. It should be noted that $\widetilde{\rho}$ represents the perturbation of the phase angle of v_{sabc} relative to that of the grid voltage v_{gabc}. The steady-state value of the phase angle (i.e., ρ_0) is determined by the real- and reactive-power flow of the system.

4) Linearized Model of the Load Subsystem: In this paper, three types of loads are studied: a squirrel-cage asynchronous machine, a series $R - L$ branch [Fig. 12(a)], and a thyristor-bridge rectifier [Fig. 12(b)]. Based on the large-signal models of the foregoing loads, the linearized model of a load can be expressed in the following generic form:

$$\frac{d}{dt}\widetilde{\mathbf{X}}_l = \mathbf{A}_l\widetilde{\mathbf{X}}_l + \mathbf{B}_l\begin{bmatrix}\widetilde{v}_{ld}\\\widetilde{v}_{lq}\end{bmatrix} + \mathbf{C}_l\widetilde{\omega} + \mathbf{D}_l\widetilde{u}_l \quad (58)$$

$$\begin{bmatrix}\widetilde{i}_{ld}\\\widetilde{i}_{lq}\end{bmatrix} = \mathbf{E}_l\widetilde{\mathbf{X}}_l \quad (59)$$

where $\widetilde{\mathbf{X}}_l, \mathbf{A}_l, \mathbf{B}_l, \mathbf{C}_l, \mathbf{D}_l$, and $\mathbf{E}_l$ have different entries and dimensions depending on the load type. $\widetilde{u}_l$ is the load-free control input of the asynchronous machine load and the rectifier load, representing the mechanical torque and the firing angle, respectively. However, the series R–L load does not have such a control input. Therefore, the entries of the corresponding matrix $\mathbf{D}_l$ are zero for the series R–L load. Similarly, $\widetilde{\omega}$ does not appear in the linearized model of the rectifier load. Consequently, the entries of $\mathbf{C}_l$ are zero for the rectifier load.

Equations (58) and (59) describe the load as a subsystem for which $\widetilde{v}_{ld}$ and $\widetilde{v}_{lq}$ are the inputs obtained from the distribution network subsystem, and $\widetilde{\omega}$ is the input obtained from the PLL subsystem. On the other hand, $\widetilde{i}_{ld}$ and $\widetilde{i}_{lq}$ are the outputs delivered to the distribution network subsystem.

5) Linearized Model of the Overall System: A linearized model of the system of Fig. 1 is developed based on (47)–(50), (51)–(53), (54)–(57), and (58) and (59). The model is derived by substituting for the output(s) of a subsystem in the relevant input(s) of another subsystem. The process yields

$$\frac{d}{dt}\widetilde{\mathbf{X}}_{sys}$$
$$= \underbrace{\begin{bmatrix} \mathbf{A}_c & \mathbf{0}_{5\times2} & \mathbf{B}_c\mathbf{F}_n & \mathbf{0}_{5\times m}\\ \mathbf{0}_{3\times5} & \mathbf{A}_{pll} & \mathbf{B}_{pll}\mathbf{F}_n & \mathbf{0}_{3\times m}\\ \mathbf{B}_n\mathbf{E}_c & (\mathbf{C}_n\mathbf{E}_{pll}+\mathbf{H}_n\mathbf{F}_{pll}) & \mathbf{A}_n & \mathbf{D}_n\mathbf{E}_l\\ \mathbf{0}_{m\times5} & \mathbf{C}_l\mathbf{E}_{pll} & \mathbf{B}_l\mathbf{E}_n & \mathbf{A}_l\end{bmatrix}}_{\mathbf{A}_{sys}}\widetilde{\mathbf{X}}_{sys}$$
$$+ \underbrace{\begin{bmatrix}\mathbf{C}_c & \mathbf{0}_{5\times1}\\\mathbf{0}_{3\times2} & \mathbf{0}_{3\times1}\\\mathbf{0}_{8\times2} & \mathbf{0}_{8\times1}\\\mathbf{0}_{m\times2} & \mathbf{D}_l\end{bmatrix}}_{\mathbf{B}_{sys}}\begin{bmatrix}\widetilde{v}_{dcref}\\\widetilde{i}_{qref}\\\widetilde{u}_l\end{bmatrix} \quad (60)$$

where m is the number of the load state variables, and

$$\widetilde{\mathbf{X}}_{sys} = \begin{bmatrix}\widetilde{\mathbf{X}}_c^T & \widetilde{\mathbf{X}}_{pll}^T & \widetilde{\mathbf{X}}_n^T & \widetilde{\mathbf{X}}_l^T\end{bmatrix}^T. \quad (61)$$

An output of interest, for example $\widetilde{v}_{dc}$, can be calculated by

$$y = \mathbf{C}_{sys}\widetilde{\mathbf{X}}_{sys} \quad (62)$$

where $\mathbf{C}_{sys}$ is the corresponding output matrix. In Section V-C, the linearized model of (60) is employed in conjunction with a sensitivity analysis to characterize the dynamics of the overall system under the proposed control strategy.

B. Model Validation and Performance Evaluation

To demonstrate the effectiveness of the proposed control strategy, a detailed switched model of the system of Fig. 1 is simulated in the PSCAD/EMTDC software environment [35]. The switched model is also used to verify the linearized model of the overall system, described by (60)–(62), which is implemented in Matlab/Simulink. The following subsections report the results of a number of case studies. The system parameters are given in Appendix B.

1) Case 1: DC-Link Voltage Step Response: Initially, the system of Fig. 1 is in a steady state, and the reference commands v_{dcref} and i_{qref} are set to 1.0 kV and zero, respectively. The feedforward compensation of the dc-link voltage controller
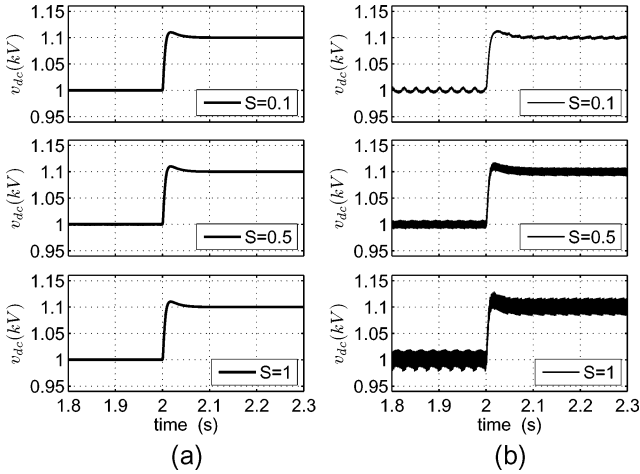
Fig. 5. Step responses of the dc-link voltage obtained from (a) the linearized model and (b) the switched model.

is also enabled (i.e., $\gamma = 1$). An asynchronous machine is connected to the middle of the distribution line. The machine is used as a generator with a mechanical torque of -0.71 p.u. to emulate a neighboring DG unit, for example, a constant-speed wind turbine. At $t = 2.0$ s, v_{dcref} is subjected to a step change to 1.1 kV. Fig. 5 illustrates the response of the dc-link voltage to the disturbance, for three irradiation levels of $S = 0.1, 0.5$, and 1.0. Columns (a) and (b) of Fig. 5 illustrate the responses obtained from the linearized and the switched models, respectively. As observed from Fig. 5, the dc-link voltage settles at 1.1 kV in less than 0.1 s. Fig. 5 demonstrates the close agreement between the linearized model and the switched model.

2) Case 2: Effectiveness of Feedforward Compensation: In this case, the system operates under the same conditions as those of Case 1, with the exception that $v_{\text{dcref}} = 1.1$ kV. At $t = 2.0$ s, v_{dcref} is reduced stepwise to 1.015 kV. Fig. 6(a) illustrates the response of v_{dc} to the disturbance when the feedforward compensation is in service. As Fig. 6(a) shows, v_{dc} tracks its reference value and settles in less than 0.1 s. On the other hand, Fig. 6(b) illustrates the response of v_{dc} when the feedforward compensation is disabled (i.e., $\gamma = 0$). It is observed that subsequent to the disturbance, v_{dc} starts to oscillate with a frequency of about 15.6 Hz. For this case, an eigenvalue analysis on (60) reveals the existence of a pair of complex-conjugate eigenvalues at $8.5 \pm 100.1j$ of which the imaginary part corresponds to a 15.9-Hz oscillatory mode. This is in close agreement with the response obtained from the switched model, shown in Fig. 6(b).

Fig. 7(a) and (b) shows the oscillations of P_s and v_{sd} when the feedforward compensation is inactive. Fig. 7(c) illustrates that the angular speed of the dq-frame (i.e., ω) also oscillates with the same frequency as those of P_s and v_{sd}. The oscillations penetrate into the distribution network and affect the asynchronous machine speed, as shown in Fig. 7(d), which may excite the torsional modes of the mechanical load. This indicates the need for the proposed feedforward compensation scheme.

C. Modal Analysis

To characterize dynamics of the PV system of Fig. 1 under the proposed control strategy of Section IV, to identify the
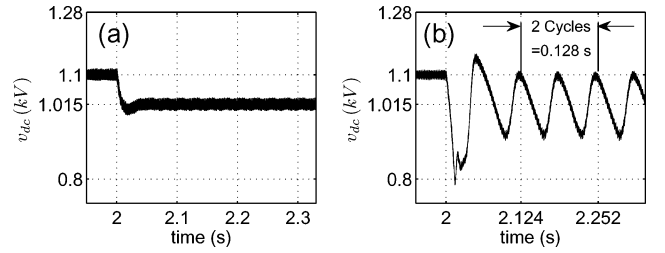

Fig. 6. Step responses of the dc-link voltage when (a) feedforward compensation is enabled and (b) feedforward compensation is disabled.
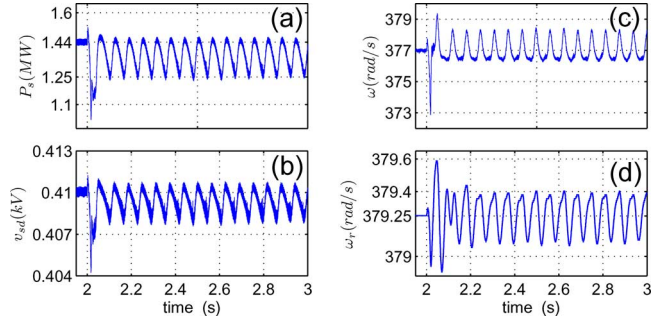

Fig. 7. PV system oscillations due to feedforward disablement.

nature of interactions between the PV system dynamics and those of the network/loads, and to determine the robustness of the proposed control against variations in various parameters, eigenvalue analysis is carried out on the linearized model of (60). For the analysis, all three types of load introduced in Section V-A4 were tested and different network/load parameters were changed. The findings indicated that under the proposed control strategy, the PV system possesses similar dynamic properties irrespective of the load type. Therefore, only the results of the asynchronous machine case are reported in what follows. Table I summarizes the essence of the system dynamic properties.

Table I includes the eigenvalues of the overall system (i.e., the solutions of $|\mathbf{A}_{\text{sys}} - \lambda_i I| = 0$ $(i = 1, 2, \ldots, 8 + 8 + m)$) under the condition that the feedforward compensation is enabled. The eigenvalues are calculated for the case that the asynchronous machine load is connected to the middle of a 15-km distribution line (i.e., $d_f = 0.5$, $S = 1$, and $v_{\text{dc}} = 1.1$ kV). In order for the asynchronous machine to represent a distributed generator, its torque is set to the negative value of -0.7 p.u. Table I shows the eight eigenvalues of the PV system, of which the first five correspond to the converter subsystem, whereas the other three are due to the PLL subsystem. For the network and the load, only the dominant (electrical) eigenvalues are included. Table I also includes the state variables of the overall system as well as a measure of the participation of each state variable in the eigenmodes corresponding to the eigenvalues.

Participation of a state variable $\tilde{x}_r$ in a mode corresponding to λ_i is calculated from [36]

$$p_{ri} = \mathbf{v}_i^r \mathbf{u}_i^r \tag{63}$$

where $\mathbf{u}_i^r$ and $\mathbf{v}_i^r$ signify the rth elements of the vectors $\mathbf{u}_i$ and $\mathbf{v}_i$, respectively $(r = 1, 2, \ldots, 8 + 8 + m)$. $\mathbf{u}_i$ and $\mathbf{v}_i$ are,

TABLE I
OVERALL SYSTEM EIGENVALUES AND STATES PARTICIPATION FACTORS; $\gamma = 1, l_e = 15$ km, $X/R = 0.6, d_f = 0.5$

			Eigenvalues of $\mathbf{A}_{sys}$ and Their Associated Subsystems								
			$\lambda_1 =$ -1350; Conv.	$\lambda_2 =$ -672; Conv.	$\lambda_3 =$ -228; Conv.	$\lambda_4 =$ -55; Conv.	$\lambda_5 =$ -2000; Conv.	$\lambda_6 =$ -132.5; PLL	$\lambda_{7,8} =$ $-219 \pm 111j$; PLL	$\lambda_{9,10} =$ $-143 \pm 8437j$; Network	$\lambda_{11} =$ $-29 \pm 0.4j$; Load
PV System States	1	i_d	0.760	0.163	0.110	0.007	0	0.007	0.007	0.007	≈ 0
	2	v_{dc}	0.020	0.620	2.090	0.044	0	0.022	0.033	≈ 0	≈ 0
	3	x_3	0.001	0.042	0.479	1.420	0	0.011	0.006	≈ 0	≈ 0
	4	x_4	0.087	1.770	0.698	0.027	0	0.004	0.011	≈ 0	≈ 0
	5	i_q	0	0	0	0	1	0	0	0	0
	6	ζ_1	0.002	0.003	0.230	≈ 0	0	0.920	1.910	0.002	≈ 0
	7	ζ_2	≈ 0	≈ 0	0.153	≈ 0	0	3.220	1.073	≈ 0	≈ 0
	8	ρ	0.001	≈ 0	0.353	≈ 0	0	3.090	2.890	0.001	0.012
Network States	9	i_{g1d}	0.329	0.033	0.010	≈ 0	0	0.001	0.002	0.006	≈ 0
	10	i_{g1q}	≈ 0	≈ 0	≈ 0	≈ 0	0	≈ 0	≈ 0	0.393	≈ 0
	11	i_{g2d}	0.034	0.003	0.001	≈ 0	0	≈ 0	≈ 0	0.003	≈ 0
	12	i_{g2q}	≈ 0	≈ 0	≈ 0	≈ 0	0	0.002	0.004	0.0913	≈ 0
	13	v_{sd}	0.007	≈ 0	≈ 0	≈ 0	0	≈ 0	≈ 0	0.014	≈ 0
	14	v_{sq}	0.001	≈ 0	≈ 0	≈ 0	0	0.001	0.001	0.456	≈ 0
	15	v_{ld}	≈ 0	≈ 0	≈ 0	≈ 0	0	≈ 0	≈ 0	0.001	≈ 0
	16	v_{lq}	≈ 0	≈ 0	≈ 0	≈ 0	0	0.001	0.002	0.032	≈ 0
Load States	17	x_{l1}	≈ 0	≈ 0	0.006	≈ 0	0	0.033	0.045	≈ 0	0.004
	18	x_{l2}	≈ 0	≈ 0	≈ 0	≈ 0	0	0.001	0.001	0.001	0.005
	19	x_{l3}	≈ 0	≈ 0	0.003	≈ 0	0	0.064	0.0521	≈ 0	0.500
	20	x_{l4}	≈ 0	≈ 0	0.001	≈ 0	0	0.005	0.003	≈ 0	0.504

respectively, the right eigenvectors of $\mathbf{A}_{\text{sys}}$ and $\mathbf{A}_{\text{sys}}^T$, corresponding to the eigenvalue λ_i. In general, $p_{ri} = a + jb$ is a complex number. However, the relative participation of a state variable in an eigenmode is of prime interest here. Hence, the norm $\|p_{ri}\| = \sqrt{a^2 + b^2}$ is reported in Table I rather than p_{ri}. The values are rounded off to the thousandths place; and any relative participation smaller than 0.001 is denoted by "≈ 0" in Table I.

Table I indicates that while the state variables of the PV system actively participate in the eigenmodes corresponding to λ_1 to λ_8, the participation of the network and load-state variables in those eigenmodes is insignificant. The only exception is the network state i_{g1d} which participates relatively actively in the eigenmode corresponding to λ_1. This, in turn, means that the PV system eigenvalues and the corresponding eigenmodes are weak functions of the network and load parameters. Therefore, if the eigenmodes of the PV system are stable by proper design of the controllers, they do not become unstable as a result of variations in the network and load parameters. The participation of i_{g1d} in the eigenmode corresponding to λ_1 cannot pose any instability complications, since this mode is very far from the imaginary axis of the s-plane. It should be noted that p_{ri} also represents the sensitivity of the eigenvalue λ_i to the element a_{rr} of the system matrix $\mathbf{A}_{\text{sys}}$ [37]. Thus, a closer look at Table I further indicates that the eigenvalues of the PV system (i.e., λ_1 to λ_8), are insensitive to those elements of A_{sys} that correspond to the network and load subsystems (i.e., a_{rr} with $r = 9, 10, \ldots, 16 + m$).

D. Sensitivity Analysis

Figs. 8–11 illustrate the patterns of variation of the real parts of the system eigenvalues, signified by σ, as functions of various parameters. For this analysis, all three types of load have been
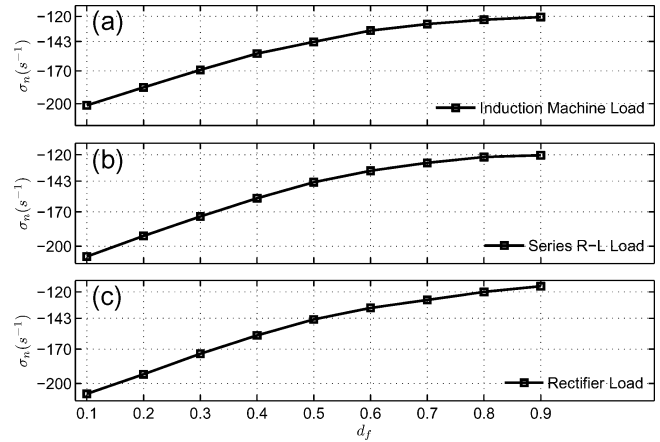

Fig. 8. Pattern of variation for real part of the network eigenvalues as a function of the normalized load distance from the PV system.

tested, and the eigenvalues with noticeable movement have been included in the plots; the other eigenvalues are almost fixed.

Fig. 8 illustrates the variation of the real part of the network eigenvalues $\lambda_{9,10}$, as a function of d_f (i.e., the normalized load distance from the PV system). Fig. 8 shows that the network eigenvalues approach the imaginary axis of the s-plane as the distance between the load and the PV system increases. Nonetheless, the corresponding mode remains stable and fast.

Fig. 9 illustrates the movements of the network eigenvalues (i.e., $\lambda_{9,10}$, and the PV system eigenvalue λ_2) as functions of the line length varying from 5 to 40 km. As Fig. 9 indicates, the network eigenmode becomes more stable, whereas the PV system eigenvalue moves slightly to the right. This, however, cannot cause any instability issues since 1) the change in the real part of λ_2 is less than 10%, and 2) λ_2 is very far from the imaginary axis of the s-plane.
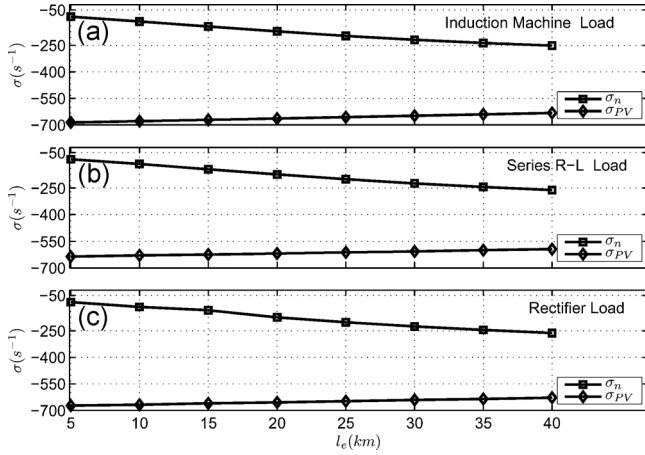
Fig. 9. Patterns of variation for real parts of two network eigenvalues and a PV system eigenvalue as functions of the line length.
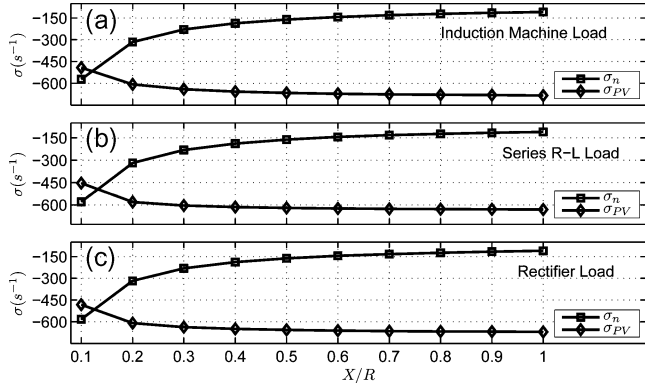

Fig. 10. Patterns of variation for real parts of two network eigenvalues and a PV system eigenvalue as functions of the line X/R ratio.
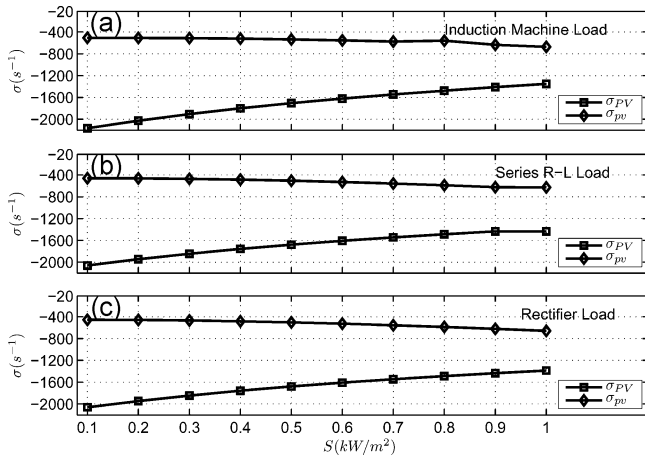

Fig. 11. Patterns of variation for real parts of two PV system eigenvalues as functions of the irradiation level.

Fig. 10 shows the variations of the network eigenvalues (i.e., $\lambda_{9,10}$) and the PV system eigenvalue λ_2 as functions of the line X/R ratio. Fig. 10 illustrates that the mode corresponding to the PV system eigenvalue becomes more stable as the X/R ratio increases, whereas the network modes exhibit opposite behavior. The movement of the network eigenvalues to the right, however,
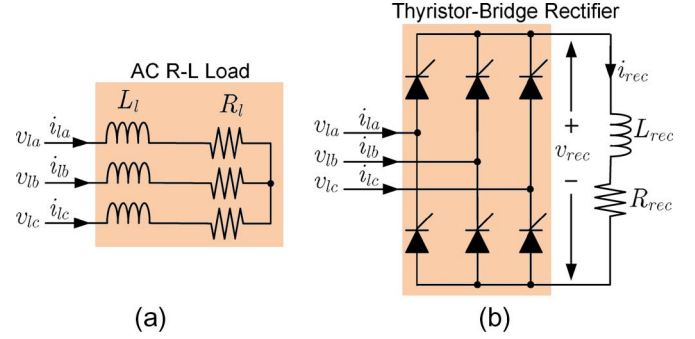

Fig. 12. Schematic diagrams of (a) R–L load and (b) rectifier load.

does not destabilize the system. The reasons are 1) $\lambda_{9,10}$ are relatively far from the imaginary axis of the s-plane, and 2) their movement rate becomes smaller as the X/R ratio increases.

The impact of the solar irradiation level on the system eigenvalues is illustrated in Fig. 11. In this case, only the PV system eigenvalues λ_1 and λ_2 are affected as S changes; the eigenvalues exhibit opposite patterns of variation. However, the corresponding eigenmodes remain stable and very fast, regardless of the irradiation level. Variation of the irradiation level exhibits no noticeable impact on the network and load eigenmodes.

VI. CONCLUSION

This paper proposes a control strategy for a single-stage, three-phase photovoltaic (PV) system that is connected to a distribution network. The proposed control strategy adopts an inner current-control loop and an outer dc-link voltage-control loop. The current-control strategy permits dc-link voltage regulation and enables power-factor control. Moreover, the current-control strategy significantly decouples dynamics of the PV system from those of the distribution network and the loads. Furthermore, it is expected that the current-control strategy renders the PV system protected against external faults. The dc-link voltage-control scheme enables the control and/or maximization of the real-power output of the PV system. This paper proposes a feedforward compensation mechanism for the dc-link voltage-control loop to mitigate the impact of the nonlinear characteristic of the PV array, to permit the design and optimization of the dc-link voltage controller for a wide range of operating conditions. The effectiveness of the control strategy is verified through digital time-domain simulation studies conducted on a detailed switched model of the overall system. In addition, a modal/sensitivity analysis is conducted on a linearized model of the system to characterize the dynamic properties of the PV system, to evaluate robustness of the controllers, and to identify the nature of interactions between the PV system and the network/loads. The results of the modal analysis confirm that under the proposed control strategy, dynamics of the PV system are decoupled from those of the distribution network. This, in turn, means that the PV system does not destabilize the distribution network. It is further demonstrated that the PV system dynamics are not influenced by the network dynamics. Thus, the PV system maintains its stability and dynamic properties despite major variations in the

TABLE II
SYSTEM PARAMETERS

PV System Parameter	Value	Comments
$Tr1$ nominal power	1.7 MVA	
$Tr1$ voltage ratio	6.6/0.48 kV	Y/Delta
$Tr1$ leakage inductance	0.1 pu	
$Tr1$ ohmic resistance	0.02 pu	
on-state resistance of valves	3 $m\Omega$	
interface inductance, L	100 μH	
interface resistance including valves resistance, R	3.0 $m\Omega$	
filter capacitance, C_f	300 μF	
switching frequency	3060 Hz	$51\times 60\ Hz$
DC-link capacitance, C	5000 μF	
# of PV cells per string, n_s	1500	
# of PV strings, n_p	176	
ideality factor, A	1.92	
cell reference temperature, ϑ_r	300 K	
temperature coefficient, k_ϑ	0.0017 A/K	
cell short circuit current, I_{scr}	8.03 A	at ϑ_r
reverse saturation current, I_{rs}	1.2×10^{-7} A	
Line Parameter	**Value**	**Comments**
grid voltage	6.6 $kVrms$	$l-l$
line inductance, $L_1 + L_2$	0.105 mH per km	
X/R ratio	0.6	
line resistance	based on L & X/R	
line length, l_e	15 km	
Machine Parameter	**Value**	**Comments**
nominal power	373 kVA	P_{base}
nominal voltage	6.6 $kVrms$	$l-l$
nominal angular frequency	377 rad/s	ω_{base}
nominal torque	989 Nm	P_{base}/ω_{base}
rotor/stator turns ratio	1.0	
number of poles	2	
stator resistance, R_s	0.0184 pu	
rotor resistance, R_r	0.0132 pu	
magnetizing inductance, L_m	3.8 pu	
stator leakage factor, σ_s	0.0223	
rotor leakage factor, σ_r	0.0223	
inertia constant, H	2.1 s	
mechanical damping, D	0.135 pu	
$R-L$ Load Parameter	**Value**	**Comments**
nominal power	373 kVA	
nominal voltage	6.6 $kVrms$	$l-l$
Inductance, L_l	95 mH	
Resistance, R	111 Ω	
Power Factor	0.95	
Rectifier Parameter	**Value**	**Comments**
nominal power	373 kVA	
nominal voltage	6.6 $kVrms$	$l-l$
DC Inductance, L_{rec}	2.0 H	
DC Resistance, R_{rec}	212 Ω	
Controller Parameter	**Value**	**Comments**
k_p (for $\tau_i = 0.5\ ms$)	0.2 Ω	
k_i (for $\tau_i = 0.5\ ms$)	0.6 Ωs^{-1}	
β_1	307.3 $1/Vs^2$	
β_2	202.9 $1/Vs^3$	
β_3	600 s^{-1}	
α_1	$-0.77\ As^{-1}/V^2$	
α_2	$-328.2\ As^{-2}/V^2$	
α_3	909 s^{-1}	

line length, line X/R ratio, load type, and distance between the PV system and the loads.

APPENDIX A
MODELS OF LOADS

1) Series R–L Load Model: Fig. 12(a) illustrates the schematic diagram of a three-phase, R–L load. Let us pick the inductor (load) current as the state variable. Thus

$$L_l\frac{d\overrightarrow{i_l}}{dt} = -R_l\overrightarrow{i_1} + \overrightarrow{v_l}. \qquad (64)$$

2) Thyristor Rectifier Model: Fig. 12(b) illustrates a schematic diagram of a thyristor-bridge rectifier supplying a series, dc, R–L load. Picking the inductor current as the state variable, one can write

$$L_{\rm rec}\frac{di_{\rm rec}}{dt} = -R_{\rm rec}i_{\rm rec} + v_{\rm rec} \qquad (65)$$

where $v_{\rm rec}$ is the rectifier dc-side voltage. It is now assumed that the rectifier operates in the continuous mode (i.e., $i_{\rm rec} > 0$), and $L_{\rm rec}$ is so large that $i_{\rm rec}$ is essentially ripple free. Thus, $v_{\rm rec}$ can be approximated by its averaged component, as

$$v_{\rm rec} \approx \overline{v_{\rm rec}} = \frac{3\sqrt{3}}{\pi}\widehat{v}_l\cos\alpha$$
$$= \frac{3\sqrt{3}}{\pi}\sqrt{\left(Re\{\overrightarrow{v_l}\}\right)^2 + \left(Im\{\overrightarrow{v_l}\}\right)^2}\cos\alpha \qquad (66)$$

where α is the firing angle, and $\widehat{v}_l$ is the magnitude of $\overrightarrow{v_l}$. Substituting for $v_{\rm rec}$ from (66) in (65), one finds

$$L_{\rm rec}\frac{di_{\rm rec}}{dt} = -R_{\rm rec}i_{\rm rec} + \frac{3\sqrt{3}}{\pi}\sqrt{\left(Re\{\overrightarrow{v_l}\}\right)^2 + \left(Im\{\overrightarrow{v_l}\}\right)^2}\cos\alpha. \qquad (67)$$

An expression for the load current can be derived by using the principle of power balance. Thus

$$\frac{3}{2}Re\{\overrightarrow{v_l}\,\overrightarrow{i_l}^*\} = i_{\rm rec}\overline{v_{\rm rec}}$$
$$= i_{\rm rec}\frac{3\sqrt{3}}{\pi}\underbrace{\sqrt{\left(Re\{\overrightarrow{v_l}\}\right)^2 + \left(Im\{\overrightarrow{v_l}\}\right)^2}}_{\widehat{v}_l}$$
$$\times \cos\alpha. \qquad (68)$$

The fundamental component of the phase current in a bridge rectifier is delayed by the angle α relative to the corresponding phase voltage [38]. It then follows from the approximation of $\overrightarrow{i_l}$ by its fundamental component that:

$$\overrightarrow{i_l} = \widehat{i}_l\frac{\overrightarrow{v_l}}{\widehat{v}_l}e^{-j\alpha} \qquad (69)$$

where $\widehat{i}_l$ is the magnitude of the space-phasor corresponding to the load (fundamental) current, and $\overrightarrow{v_l}/\widehat{v}_l$ is the unit vector collinear with $\overrightarrow{v_l}$. The substitution of $\overrightarrow{i_l}$ from (69) in (68), and simplification of the result in view of $\overrightarrow{v_l}\,\overrightarrow{v_l}^* = \widehat{v}_l^2$ yields

$$\widehat{i}_l = \frac{2\sqrt{3}}{\pi}i_{\rm rec}. \qquad (70)$$

Substituting for $\widehat{i_l}$ from (70) in (69), one deduces

$$\vec{i_l} = \left(\frac{2\sqrt{3}}{\pi}\right)\frac{\vec{v_l}}{\widehat{v_l}}e^{-j\alpha}i_{\mathrm{rec}}$$

$$= \left(\frac{2\sqrt{3}}{\pi}\right)\frac{\vec{v_l}}{\sqrt{\left(Re\{\vec{v_l}\}\right)^2 + \left(Im\{\vec{v_l}\}\right)^2}}e^{-j\alpha}i_{\mathrm{rec}}. \quad (71)$$

Equations (67) and (71) constitute a state-space model for the thyristor-bridge rectifier load.

APPENDIX B
SYSTEM PARAMETERS

The system parameters are presented in Table II.

REFERENCES

[1] H. L. Willis and W. G. Scott, *Distributed Power Generation: Planning and Evaluation.* New York: Marcel Dekker, 2000.

[2] M. Oprisan and S. Pneumaticos, "Potential for electricity generation from emerging renewable sources in Canada," in *Proc. IEEE EIC Climate Change Technology Conf.*, May 2006, pp. 1–9.

[3] J. J. Bzura, "The New England electric photovoltaic systems research and demonstration project," *IEEE Trans. Energy Convers.*, vol. 5, no. 2, pp. 284–289, Jun. 1990.

[4] J. J. Bzura, "Performance of grid-connected photovoltaic systems on residences and commercial buildings in New England," *IEEE Trans. Energy Convers.*, vol. 7, no. 1, pp. 79–82, Mar. 1992.

[5] I. Abouzahr and R. Ramakumar, "An approach to assess the performance of utility-interactive photovoltaic systems," *IEEE Trans. Energy Convers.*, vol. 8, no. 2, pp. 145–153, Jun. 1993.

[6] T. Esram and P. L. Chapman, "Comparison of photovoltaic array maximum power point tracking techniques," *IEEE Trans. Energy Convers.*, vol. 22, no. 2, pp. 434–449, Jun. 2007.

[7] H. Haeberlin, "Evolution of inverters for grid connected PV systems from 1989 to 2000," in *Proc. Photovoltaic Solar Energy Conf.*, 2001, pp. 426–430.

[8] S. B. Kjaer, J. K. Pedersen, and F. Blaabjerg, "A review of single-phase grid-connected inverters for photovoltaic modules," *IEEE Trans. Ind. Appl.*, vol. 41, no. 5, pp. 1292–1306, Sep./Oct. 2005.

[9] Y. Huang, J. Wang, F. Z. Peng, and D. Yoo, "Survey of the power conditioning system for PV power generation," presented at the Power Electronics Specialist Conf., Jeju, Korea, Jun. 2006, 6 pages.

[10] J. M. Carrasco, L. G. Franquelo, J. T. Bialasiewicz, E. Galvan, R. C. P. Guisado, M. A. M. Prats, J. I. Leon, and N. Moreno-Alfonso, "Power-electronic systems for the grid integration of renewable energy sources: A survey," *IEEE Trans. Ind. Electron.*, vol. 53, no. 4, pp. 1002–1016, Aug. 2006.

[11] G. Kern, "SunSine300: Utility interactive ac module anti-islanding test results," in *Proc. IEEE Photovoltaic Specialists Conf.*, 1997, pp. 1265–1268.

[12] Y. Noda, T. Mizuno, H. Koizumi, K. Nagasaka, and K. Kurokawa, "The development of a scaled-down simulator for distribution grids and its application for veryfying interference behavior among a number of module integrated converters (MIC)," in *Proc. IEEE Photovoltaic Specialists Conf.*, May 2002, pp. 1545–1548.

[13] A. Woyte, R. Belmans, and J. Nijs, "Testing and islanding protection function of photovoltaic inverters," *IEEE Trans. Energy Convers.*, vol. 18, no. 1, pp. 157–162, Mar. 2003.

[14] L. A. C. Lopes and H. Sun, "Performance assessment of active frequency drifting islanding detection methods," *IEEE Trans. Energy Convers.*, vol. 21, no. 1, pp. 171–180, Mar. 2006.

[15] G. L. Campen, "An analysis of the harmonics and power factor effects at a utility intertied photovoltaic system," *IEEE Trans. Power App. Syst.*, vol. PAS 101, no. 12, pp. 4632–4639, Dec. 1982.

[16] J. H. R. Enslin and P. J. M. Heskes, "Harmonic interaction between a large number of distributed power inverters and the distribution network," *IEEE Trans. Power Electron.*, vol. 19, no. 6, pp. 1586–1593, Nov. 2004.

[17] M. C. Benhabib, J. M. A. Myrzik, and J. L. Duarte, "Harmonic effects caused by large scale PV installations in LV network," presented at the Int. Conf. Electrical Power Quality and Utilization, Barcelona, Spain, Oct. 2007, 6 pages.

[18] N. Srisaen and A. Sangswang, "Effect of pv grid-connected system location on a distribution system," in *Proc. IEEE Asia Pacific Conf. Circuit and Systems*, Dec. 2006, pp. 852–855.

[19] A. Woyte, V. Van Thong, R. Belmans, and J. Nijs, "Voltage fluctuations on distribution level introduced by photovoltaic systems," *IEEE Trans. Energy Convers.*, vol. 21, no. 1, pp. 202–209, Mar. 2006.

[20] M. Thomson and D. G. Infield, "Impact of widespread photovoltaics generation on distribution systems," *Inst. Eng. Technol. J. Renew. Power Gen.*, vol. 1, no. 1, pp. 33–40, Mar. 2007.

[21] L. Wang and Y. Lin, "Dynamic stability analysis of photovoltaic array connected to a large utility grid," in *Proc. IEEE Power Eng. Soc. Winter Meeting*, Jan. 2000, vol. 1, pp. 476–480.

[22] M. Liserre, R. Teodorescue, and F. Blaabjerg, "Stability of photovoltaic and wind turbine grid-connected inverters for a large set of grid impedance values," *IEEE Trans. Power Electron.*, vol. 21, no. 1, pp. 263–272, Jan. 2006.

[23] B. Rodriguez and G. A. J. Amartunga, "Dynamic stability of grid-connected photovoltaic systems," in *Proc. IEEE Power Eng. Soc. General Meeting*, Jun. 2004, vol. 2, pp. 2193–2199.

[24] T. Ostrem, W. Sulkowski, L. E. Norum, and C. Wang, "Grid connected photovoltaic (PV) inverter with robust phase-locked loop (PLL)," presented at the IEEE/Power Eng. Soc. Transmission Distribution Conf. Expo., Caracas, Venezuela, Aug. 2006.

[25] O. Wasynczuk and N. A. Anwah, "Modeling and dynamic performance of a self-commutated photovoltaic inverter system," *IEEE Trans. Energy Convers.*, vol. 4, no. 3, pp. 322–328, Sep. 1989.

[26] S. Zheng, P. Wang, and L. Ge, "Study on pwm control strategy of photovoltaic grid-connected generation system," in *Proc. IEEE Int. Conf. Power Electronics and Motion Control*, Shanghai, China, Aug. 2006, vol. 3.

[27] E. Figueres, G. Garcera, J. Sandia, and F. J. Gonzalez-Espin, "Modelling and control of a 100 kW photovoltaic inverter with an LCL grid filter for distributed power systems," in *Proc. Eur. Conf. Power Electronics and Applications*, Aalborg, Denmark, Sep. 2007.

[28] W. Libo, Z. Zhengming, and L. Jianzheng, "A single-stage three phase grid-connected photovoltaic system with modified MPPT method and reactive power compensation," *IEEE Trans. Energy Convers.*, vol. 22, no. 4, pp. 881–886, Dec. 2007.

[29] K. H. Hussein, I. Muta, T. Hoshino, and M. Osakada, "Maximum photovoltaic power tracking: An algorithm for rapidly changing atmospheric conditions," *Proc. Inst. Elect. Eng., Gen., Transm., Distrib.*, vol. 142, no. 1, pp. 59–64, Jan. 1995.

[30] A. Yazdani and R. Iravani, "An accurate model for the dc-side voltage control of the neutral point diode clamped converter," *IEEE Trans. Power Del.*, vol. 21, no. 1, pp. 185–193, Jan. 2006.

[31] P. Vas, *Vector Control of AC Machines.* Oxford, U.K.: Oxford Univ. Press, 1990.

[32] W. Leonhard, *Control of Electrical Drives*, 3rd ed. New York: Springer, 2001.

[33] S. K. Chung, "A phase tracking system for three phase utility interface inverters," *IEEE Trans. Power Electron.*, vol. 15, no. 3, pp. 431–438, May 2000.

[34] C. Schauder and H. Mehta, "Vector analysis and control of advanced static VAR compensators," *Proc. Inst. Elect. Eng., Gen., Transm., Distrib.*, vol. 140, no. 4, pp. 299–306, Jul. 1993.

[35] PSCAD/EMTDC v. 4.2 Manitoba HVDC Research Centre. Winnipeg, MB, Canada.

[36] P. Kundur, *Power System Stability and Control.* New York: McGraw-Hill, 1994.

[37] B. Porter and T. R. Crossley, *Modal Control: Theory and Applications.* London, U.K.: Taylor & Francis, 1972.

[38] K. Thorborg, *Power Electronics.* Upper Saddle River, NJ: Prentice-Hall, 1988.

Amirnaser Yazdani (S'02–M'05) received the Ph.D. degree in electrical engineering from the University of Toronto, Toronto, ON, Canada, in 2005.

He was with Digital Predictive Systems (DPS) Inc., Mississauga, ON, Canada. Currently, he is an Assistant Professor with the University of Western Ontario (UWO), London. His research interests include modeling and control of switching power converters, distributed generation, and microgrids.

Prajna Paramita Dash (S'08) received the B.Sc. degree in electrical engineering from the National Institute of Technology, Rourkela, Rourkela, India.

She joined the University of Western Ontario, London, ON, Canada, in 2007, where she is currently pursuing the M.E.Sc. degree. Her research interests include distributed generation, renewable energy, and power systems.